# Controlling antiferromagnetic domains in patterned $La_{0.7}Sr_{0.3}FeO_3$ thin films

Michael S. Lee[1], Peifen Lyu[1], Rajesh V. Chopdekar[1,2], Andreas Scholl[2], Scott T. Retterer[3], and Yayoi Takamura[1,*]

[1] Department of Materials Science and Engineering, University of California, Davis, Davis, CA, USA, 95616

[2] Advanced Light Source, Lawrence Berkeley National Laboratory, Berkeley, CA, USA, 94703

[3] Center for Nanophase Materials Sciences, Oak Ridge National Laboratory, Oak Ridge, TN, USA, 37831

**Abstract**

Transition metal oxide thin films and heterostructures are promising platforms to achieve full control of the antiferromagnetic (AFM) domain structure in patterned features as needed for AFM spintronic devices. In this work, soft x-ray photoemission electron microscopy was utilized to image AFM domains in micromagnets patterned into $La_{0.7}Sr_{0.3}FeO_3$ (LSFO) thin films and $La_{0.7}Sr_{0.3}MnO_3$ (LSMO)/LSFO superlattices. A delicate balance exists between magnetocrystalline anisotropy, shape anisotropy, and exchange interactions such that the AFM domain structure can be controlled using parameters such as LSFO and LSMO layer thickness, micromagnet shape, and temperature. In LSFO thin films, shape anisotropy gains importance only in micromagnets where at least one extended edge is aligned parallel to an AFM easy axis. In contrast, in the limit of ultrathin LSFO layers in the LSMO/LSFO superlattice, shape anisotropy effects dominate such the AFM spin axes at micromagnet edges can be aligned along any in-plane crystallographic direction.

*corresponding author: ytakamura@ucdavis.edu

**Introduction**

The burgeoning field of antiferromagnetic (AFM) spintronics has received a surge of interest after recent groundbreaking results such as the successful experimental demonstration of electrical switching and readout of AFM CuMnAs between stable configurations using an applied current.[1] Until that time, the net zero magnetization of AFM materials limited their applications, primarily due to the difficulty to probe their magnetic properties, and their relative insensitivity to applied magnetic fields. However, these apparent disadvantages can also be considered as advantages for AFM device applications as they result in the stability of the AFM state to applied magnetic fields and ensure that no stray fields are generated from AFM features.[2-5] Furthermore, theoretical predictions show that AFM materials may enable fundamentally faster device operation compared to comparable ferromagnetic (FM) materials due to high-frequency magnons.[6-8]

The use of transition metal oxides for AFM spintronics is appealing because their functional properties can be sensitively manipulated by a variety of external stimuli such as lattice strains, optical illumination, or applied magnetic or electric fields.[9] Furthermore, modern film growth techniques offer the ability to control chemical composition and thickness of layers with atomic level precision enabling the synthesis of complex epitaxial heterostructures which harness interfacial coupling interactions. For example, the family of Sr-doped lanthanum ferrites (i.e. $La_{1-x}Sr_xFeO_3$) are G-type AFM insulators and the Néel temperature, $T_N$, decreases with increasing Sr-doping level, $x$. When grown epitaxially on $SrTiO_3$ (STO) substrates, $La_{1-x}Sr_xFeO_3$ thin films exist under a small compressive strain and exhibit four types of AFM domains where their spin axes cant out-of-plane by ~ 30 ° with an in-plane projection along the <100> substrate directions.[10-12] While the locations of AFM domains typically occur stochastically, largely influenced by the presence of defects with pin the locations of domain walls,[13] the nature of AFM domains in $La_{1-x}Sr_xFeO_3$ thin films can be modified using exchange interactions with adjacent FM layers. For example, the (001) interface between $La_{1-x}Sr_xFeO_3$ and $La_{1-x}Sr_xMnO_3$ layers was shown to display spin-flop coupling characterized by a direct correlation between the FM and AFM domains with a perpendicular alignment between the FM and AFM spin axes.[10, 14-18] For a [6 u.c. $La_{0.7}Sr_{0.3}MnO_3$ (LSMO)][6 u.c. $La_{0.7}Sr_{0.3}FeO_3$ (LSFO)]$_{10}$ superlattice, the AFM spin axes was confined to lie within the plane of the film along the <100> substrate directions, rather than canting out-of-plane.

Additionally, the AFM spin axes could be rotated within the film plane with a moderate value of applied magnetic field ($\boldsymbol{H}$=0.3 T) through a torque from the FM LSMO layer.[19] This spin-flop coupling was only observed for a small range of $La_{1-x}Sr_xFeO_3$ thicknesses, as the $La_{1-x}Sr_xFeO_3$ layer loses its AFM properties below a critical thickness around three unit cells, while the $La_{1-x}Sr_xFeO_3$ anisotropy dominates over the spin-flop coupling for thicknesses greater than 18 unit cells.[20] Similarly, the direction of the AFM spin axes in the $La_{1-x}Sr_xFeO_3$ layers was found to depend sensitively on the layer thickness.[10, 21] In other work, canted FM moments were observed on the $LaFeO_3$ layer of LSMO/$LaFeO_3$/LSMO heterostructures with an antiparallel orientation to the LSMO magnetization, which strongly impacted the tunneling magnetoresistance.[22]

Due to the lack of magnetostatic energy in AFM materials from the absence of magnetic dipoles terminating on the surfaces of features, micro-/nanoscale patterning of AFM materials are not expected to exhibit any shape anisotropy effects.[23, 24] However, shape anisotropy effects are theoretically predicted to result from magnetoelastic forces and surface magnetic anisotropy,[25, 26] and have indeed been observed in in single-crystalline NiO/Fe and CoO/Fe discs through imprinting from the FM Fe layer[27] as well as $La_{1-x}Sr_xFeO_3$ and $La_{1-x}Sr_xFeO_3$/LSMO micro-/nanoscale features that were defined using an $Ar^+$ ion implantation-based patterning technique.[17, 21, 28-34] This technique results in magnetic islands embedded within a non-magnetic matrix, and it is postulated that these edge effects result from a lateral compressive strain imposed onto the magnetic islands from the surrounding matrix.[35] Soft x-ray photoemission electron microscopy (X-PEEM) remains one of the few imaging techniques capable of directly imaging AFM domains in thin films by taking advantage of the x-ray magnetic linear dichroism (XMLD) effect. In this work, we performed a detailed investigation of the competing interactions of shape anisotropy and AFM magnetocrystalline anisotropy effects by imaging the AFM domains using X-PEEM for a wide range of patterned samples and $La_{0.7}Sr_{0.3}FeO_3$ (LSFO) layer thickness ranging from 6 to 90 unit cells. In the ultrathin limit, LSFO layers with six unit cell thickness were confined between LSMO layers with six unit cells thickness, repeated 10 times in a superlattice structure (i.e. [6 u.c. LSMO][6 u.c. $LSFO]_{10}$ superlattice). Due to interfacial charge transfer,[36] the Curie temperature, $T_C$, of the LSMO layer is reduced to ~50 K, while the LSFO Néel temperature, $T_N$, is increased above 400 K.[19] Taking advantage of the disparate critical temperatures,

we can directly compare the AFM domain structure ultrathin LSFO layers separated by, paramagnetic spacer layers imaged at 105 K or 300 K, to the same ultrathin LSFO layers which experience spin-flop coupling with FM LSMO layers at 36 K. This ability to readily control the AFM domain structure is imperative for the implementation of AFM spintronic devices.

**Methods**

The LSFO film and LSMO/LSFO superlattice were deposited epitaxially on (001)-oriented 0.1% Nb-doped STO substrates by pulsed laser deposition. A KrF (248 nm) laser was operated at a frequency of 10 Hz and an energy density of approximately 1 J/cm$^2$ while the substrate was heated to 700°C in an oxygen atmosphere of 200 mTorr. The sample was cooled in 300 Torr $O_2$ in order to ensure proper oxygen stoichiometry in the layers. X-ray diffraction and resonant x-ray reflectivity measurements confirm the high degree of crystallinity of the epitaxial films, and their individual layer thicknesses. The patterned micromagnets were defined using an electron-beam lithography-deposited Cr hard mask, with a subsequent $Ar^+$ flood ion implantation (50 keV implant energy and 1x10$^{15}$ cm$^{-2}$ dose) to locally modify the structural order throughout the film thickness in the regions not protected by the mask.[28, 29] This technique creates magnetically active islands of arbitrary shape and size embedded in the implanted/non-magnetic matrix.

The AFM domain images were obtained using X-PEEM performed using the PEEM3 microscope at beamline 11.0.1 at the Advanced Light Source.[37] Due to the finite electron escape depth of the secondary electrons imaged in the PEEM3 microscope, the imaging is limited to the top 5-10 nm of the sample surface,[38] however, prior measurements on LSMO/LSFO heterostructures showed excellent agreement between the surface and bulk properties.[16, 20] AFM domain contrast results from the XMLD signal at the Fe *L*-edge. The measurement geometry is shown in Fig. 1(a) where the linearly polarized x-rays were incident upon the sample at a grazing incident angle of 30 ° and a series of images were acquired from the same sample location while the x-ray ***E***-vector was rotated from *p*- to *s*-polarization in increments of 10 ° (or 30 ° in the case of triangle and pentagon shapes). The linear polarization angle, $\beta$, was defined to be 0 ° (90 °) for *p*- (*s*-) polarized x-rays, respectively, where for *s*-polarization, the ***E***-vector lies in the plane of the sample, and for *p*-polarization, the ***E***-vector cants out-

of-plane by 30 °. The XMLD intensity can be expressed by Equation 1, where $a$ and $b$ are constants, $\boldsymbol{L}$ is the AFM moment, and $\theta$ is the angle between $\boldsymbol{L}$ and the $\boldsymbol{E}$-vector of the linearly polarized x-rays [39].

$$I(\theta) = a + b(3\ cos^2\theta - 1) \langle L^2 \rangle \qquad \text{EQN (1)}$$

For LSFO, the XMLD spectra is characterized by positive/negative features at the A/B multiplet features of the Fe $L_3$ and $L_2$ edges.[39] AFM domain images were calculated using an asymmetry operation between two X-PEEM images, each normalized by an image taken at a pre-edge energy, collected with a given $\beta$ value and x-ray energies corresponding to the Fe $L_2$ A/B multiplet features. The asymmetry operation effectively eliminates image contrast due to local topographical and work function differences, leaving only the AFM contributions. The intensity of each pixel in the domain image was extracted as a function of $\beta$ angle and its AFM domain orientation was assigned by comparison to calculated XMLD intensity curves using Equation 1 for various AFM spin axis orientations and the known experimental geometry.[10, 21, 32] This process was performed for two sample orientations relative to the incident x-rays (i.e. with the projection of the x-rays along the in-plane <100> and <110> substrate directions).

FM domain contrast from the LSMO sublayers results from x-ray magnetic circular dichroism (XMCD) at the Mn $L_{3,2}$ absorption edge, where the contrast intensity is proportional to the cosine of the angle between local FM moment orientation and the incident x-ray helicity vector. An asymmetry operation was performed using normalized images acquired using right/left circularly polarized x-rays at the x-ray energy corresponding to the maximum XMCD at the Mn $L_3$ absorption edge.

A variety of shapes were utilized to capture the balance between shape and magnetocrystalline anisotropies of the LSFO micromagnets. Two types of squares were investigated with an edge length of 2 μm which were aligned along either the in-plane <100> and <110> substrate directions. Circles were defined with a diameter of 2 μm while triangles and pentagons had a height of 2 μm. Each shape was repeated 225 times on the sample with nine micromagnets imaged at a resolution adequate for the XMLD analysis. Only a single micromagnet is shown for each shape, but they are representative of all micromagnets studied.

**Results and Discussion**

Fig. S1 shows Fe edge XMLD-PEEM images acquired at 300 K as a function of $\beta$ for a representative square LSFO micromagnet with its edges along the in-plane <100> substrate directions. For each image, regions of white, grey, and black contrast can be observed, and each region possesses its own unique $\beta$ dependence. For example, the domain at the left of the micromagnet has dark contrast for $\beta = 0$ ° and becomes progressively brighter as $\beta$ increases. In contrast, the domain along the bottom edge of the square has a broad minimum in contrast for $\beta \sim 60$ °. The XMLD image with $\beta = 60$ ° provides the largest domain contrast between domain types and will be used as the representative image for the other micromagnet shapes. Fig. 1(b) plots the collective $\beta$ dependence of each pixel in the series of images shown in Fig. S1. Four distinct trends can be observed, corresponding to four types of AFM domains which differ by the orientation of the AFM spin axis. The error bars correspond to the standard deviation of all pixels within a domain type.

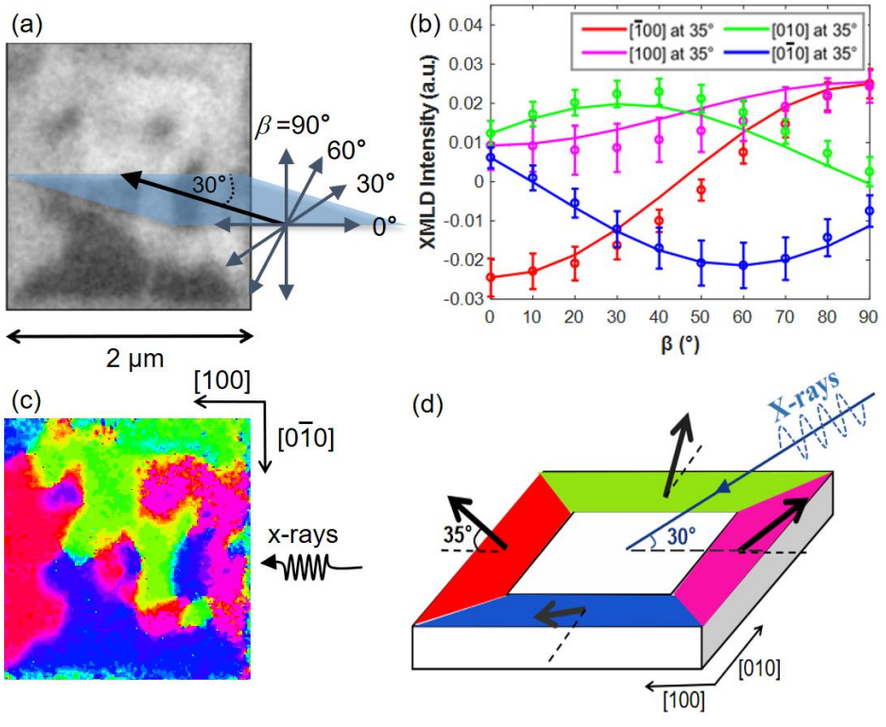


**Figure 1.** Analysis of AFM domain images at 300 K for square LSFO micromagnets with edges along the <100> substrate directions and x-rays incident parallel to the [100] substrate direction. (a) XMLD measurement geometry. (b) Experimental (symbols) and calculated (solid line) Fe XMLD intensity vs. $\beta$ for the four AFM domains. The error bars correspond to the standard deviation of all pixels within a domain type. (c) AFM domain map of the

same micromagnet as in Fig. S1. (d) Schematic of the four AFM domains in which their spin axes have an in-plane projection along the <100> substrate directions and a canting angle of 35 ° +/- 5 °.

The assignment of the AFM spin axis in each domain was performed by matching the experimental XMLD intensity vs. $\beta$ curve to calculated XMLD curves taking into account the measurement geometry and a known AFM spin axis orientation. Each pixel in the XMLD-PEEM images was assigned to a domain type and an AFM domain map was constructed as shown in Fig. 1(c). For the analysis, results from unpatterned $La_{1-x}Sr_xFeO_3$ thin films were used as a starting point, where the AFM spin axes were found to cant out-of-plane by 30 ° with the in-plane projection along the <100> substrate directions.[10-12, 24] In this case, the XMLD intensity of the four AFM domains was best fit with an out-of-plane canting angle of 35 ° +/- 5 ° relative to the sample surface. The center of all the patterned micromagnets show a random pattern of the four domain types with ~0.3 μm diameter, however they all show a preferential edge alignment of the AFM spin axis within ~0.3 μm of the perimeter such that the spin axis lies *perpendicular* to the edge of the micromagnet (see schematic in Fig. 1(d)). Furthermore, the domain walls tend to be pinned at the corners of the micromagnets. Confirmation of the AFM spin axis orientations was obtained by rotating the LSFO micromagnets relative to the x-ray propagation direction so that the x-rays were incident parallel to the in-plane [110] substrate direction while the edges remain oriented parallel to the in-plane <100> substrate directions. A good fit between the experimental and calculated XMLD vs. $\beta$ curves was obtained using the same AFM spin axis model and this measurement geometry (see Figure S2).

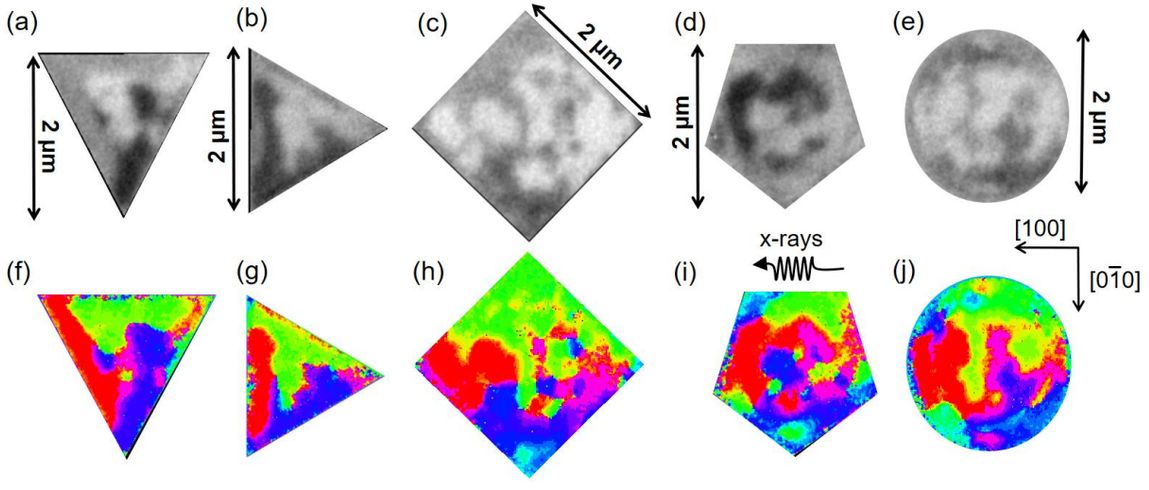


**Figure 2.** (a) – (e) Fe XMLD-PEEM images at 300 K for $\beta$ = 60° and (f) – (j) AFM domain maps of LSFO

micromagnets with varying shapes. Colors are as defined in Fig. 1 and denote the four types of AFM domains in which their spin axes have an in-plane projection along the <100> directions and a canting angle of 35 ° +/- 5 °.

In order to separate the effect of shape anisotropy from magnetocrystalline anisotropy, LSFO micromagnets of varying shape were investigated, including triangle, square (edges parallel to in-plane <110> substrate directions), pentagon, and circle shapes. Figure 2 shows Fe XMLD-PEEM images for $\beta = 60$ ° and AFM domain maps while Fig. S3 shows the associated XMLD intensity vs. $\beta$ curves for these shapes. Pixel-by-pixel analysis identifies the same four types of AFM domains in which their spin axis cant out-of-plane by 35° +/- 5° with their in-plane projections along the <100> substrate directions. The general location of each type of domain remains the same regardless of the shape and uniformly for the nine micromagnets images at high resolution, with the green/blue domains at the top/bottom of micromagnets, and the red/magenta domains on the left/right sides. Furthermore, in comparing the triangle, square with edges along the <110> substrate directions, and pentagon micromagnets with three, four, and five corners, respectively, a trend of increasing complex domain structure can be observed with increasing number of corners. The triangle is formed primarily of only three domains (green, red, and blue) which originate at the edges of the micromagnet and propagate almost throughout the entire volume. This behavior remains regardless of whether one of the edges lies along the [100] or [010] substrate direction. In contrast, the volume of the pentagon and circle micromagnets are composed almost exclusively by the smaller 0.3 μm diameter domains in a random fashion. These results suggest that a delicate balance exists between shape anisotropy and magnetocrystalline anisotropy in these micromagnets with 2 μm dimensions. Magnetocrystalline anisotropy dominates in the center of the micromagnets regardless of shape and the AFM easy spin axes have their projections along the <100> substrate directions. Magnetocrystalline anisotropy also dominates for shapes with proportionally fewer edges aligned parallel to the easy axes (pentagons, circles, and squares with edges along the <110> substrate directions). Shape-dependent edge effects only become important when at least one of extended edges of the micromagnets are aligned parallel to an easy axis (triangles and squares with edges along the <100> substrate directions).

The types of AFM domains observed in the patterned micromagnets was modified by the confinement

of ultrathin LSFO layers between paramagnetic LSMO spacer layers at temperature above $T_C$ and below $T_N$. Images were captured at both 105 K and 300 K with similar results at both temperatures. Figure S4 shows the series of Fe edge XMLD-PEEM images at both temperatures as a function of $\beta$ for a representative square LSFO/LSMO micromagnet with its edges along the in-plane <100> substrate directions. Unlike the case of the LSFO micromagnet, the strongest domain contrast is observed for $\beta$ = 90 ° and it slowly decreases as $\beta$ decreases such that almost no domain contrast can be observed for $\beta$ = 0 °. As the x-ray ***E***-vector lies completely in plane for $\beta$ = 90 °, these images are most sensitive to in-plane AFM spin axes with the brightest and darkest regions corresponding to [100] and [010] domains, respectively. Furthermore, the absence of any domain contrast for $\beta$ = 0 ° suggests that no out-of-plane component exists in this type of micromagnet. The pixel-by-pixel analysis in Fig. 3 at 105 K (Fig. S5 at 300 K) confirms that only two types of AFM domains exist and that they are confined to lie completely in-plane along the [100] and [010] substrates directions, corresponding to the magenta and green domains in the domain maps, respectively. This orientation of the AFM spin axes agrees with unpatterned LSMO/LSFO superlattices with equivalent layer thicknesses.[10, 16] The location of the domains are such that the AFM spin axis lies *perpendicular* to the edges of the micromagnets and these edge domains extend into the interior of the micromagnet such that it is composed of only two domains of each type. A few pixels shown in grey, do not conform to the expected $\beta$ dependence of these domains. These pixels are predominantly located at the boundaries between domains, and therefore constitute the domain walls. The measured domain wall width is 0.15-0.2 μm, which is close to the PEEM3 microscope spatial resolution for this type of sample, and therefore the XMLD intensity vs. $\beta$ spectra for those pixels cannot be accurately modeled.

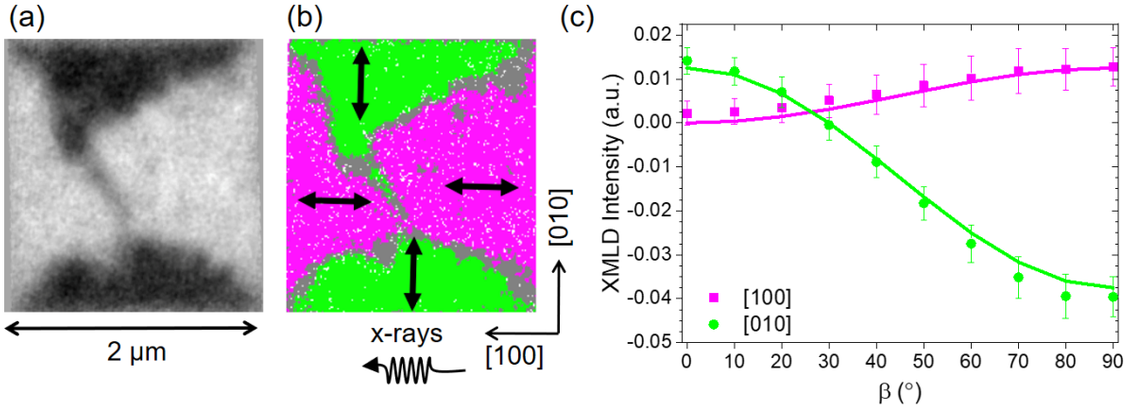

**Figure 3**: Analysis of AFM domain images at 105 K for square LSMO/LSFO micromagnets with edges along the <100> substrate directions and x-rays incident parallel to the [100] substrate direction. (a) Fe XMLD-PEEM image with $\beta = 90°$. (b) AFM domain map where the arrows denote the orientation of the AFM spin axis along the in-plane [100] and [010] substrate directions. The grey pixels at the domain walls display a $\beta$ dependence distinct from either of the two domains. (c) Experimental (symbols) and calculated (solid line) XMLD intensity vs. $\beta$ curves for the two AFM domains.

Alternative micromagnet shapes were also investigated in the LSMO/LSFO superlattice to separate the effect of shape anisotropy and magnetocrystalline anisotropy. Fig. 4 shows the results from the domain analysis for circle and square micromagnets with edges along the <110> substrate directions, shapes which do not have edges aligned parallel to the AFM easy axes. The analysis of these micromagnets shows nearly all pixels in the micromagnets can be categorized as one of four distinct domains with their AFM spin aligned along either the in-plane $[100]$, $[010]$, $[110]$, or $[1\bar{1}0]$ substrate directions, with some ambiguity in domain assignment at domain walls. For both shapes, the interior of the micromagnets consist of irregular shaped domains with their spin axes aligned along the $[100]$ and $[010]$ substrate directions, consistent with magnetocrystalline anisotropy. These domains appear with strong dark/bright contrast in the Fe edge XMLD-PEEM images with $\beta = 90°$ shown in Fig. 4. However, the micromagnet perimeter uniformly appears with grey contrast within 0.30 μm of the edge of the micromagnet (Fig. S6). The pixel-by-pixel analysis for two sample orientations with the x-ray incident along the [100] and [110] substrate directions (Fig. 4 and Fig. S7, respectively) shows that these perimeter regions correspond to $[110]$ and $[1\bar{1}0]$ domains such that the AFM spin axes are always oriented *perpendicular* to the edges. These domains extend across the entire 2 μm edge of the square micromagnet and the domain walls are pinned at the corners. While this type of AFM domain pattern has also been observed in spin-flop coupled system when a thick LSMO layer displayed a FM Landau state [30], in this case, no Fe or Mn XMCD was observed at 300 K for any shape. For the circle micromagnet, the domains near the edge appear less abrupt, represented by the speckled nature of the AFM domain map in Fig. 4(e) constructed with the simple assumption of four AFM domain types. Fig. S8 shows that the intensity of the Fe XMLD-PEEM image with $\beta = 90°$ around the circumference of the circle micromagnet follows a $cos^2(\theta)$ dependence which is consistent with a gradual rotation of the

AFM spin axis to maintain a perpendicular alignment with the micromagnet edge. If clear domains were present, abrupt changes in XMLD intensity would be observed as a function of angle.

Therefore, despite the fact that shape anisotropy driven by magnetostatic effects are not expected in AFM domains, LSFO micromagnets patterned into an LSFO thin film and LSMO/LSFO superlattice display clear shape anisotropy effects. For the 90 u.c LSFO thin film, these effects dominate in shapes with fewer corners where at least one extended edge lies parallel to the AFM easy axis such that extended domains form along the micromagnet perimeter with their spin axes oriented perpendicular to the edge. Away from the perimeter (distances < 0.30 μm) and in shapes with edges not aligned with the AFM easy axis, magnetocrystalline anisotropy dominates with the formation of small AFM domains. The magnetic easy axes cant out-of-plane by 35° +/- 5° with their in-plane projections along the <100> substrate directions, consistent with previous measurements on unpatterned $La_{1-x}Sr_xFeO_3$ thin films. [10-12, 24] Confinement of an ultrathin LSFO layer in an LSMO/LSFO superlattice forces the magnetic easy axis to lie completely in-plane along the <100> substrate directions, and it enables shape anisotropy effects to dominate over magnetocrystalline anisotropy near the micromagnet edges as AFM spin axes align along any in-plane direction to satisfy a perpendicular orientation to the edge.

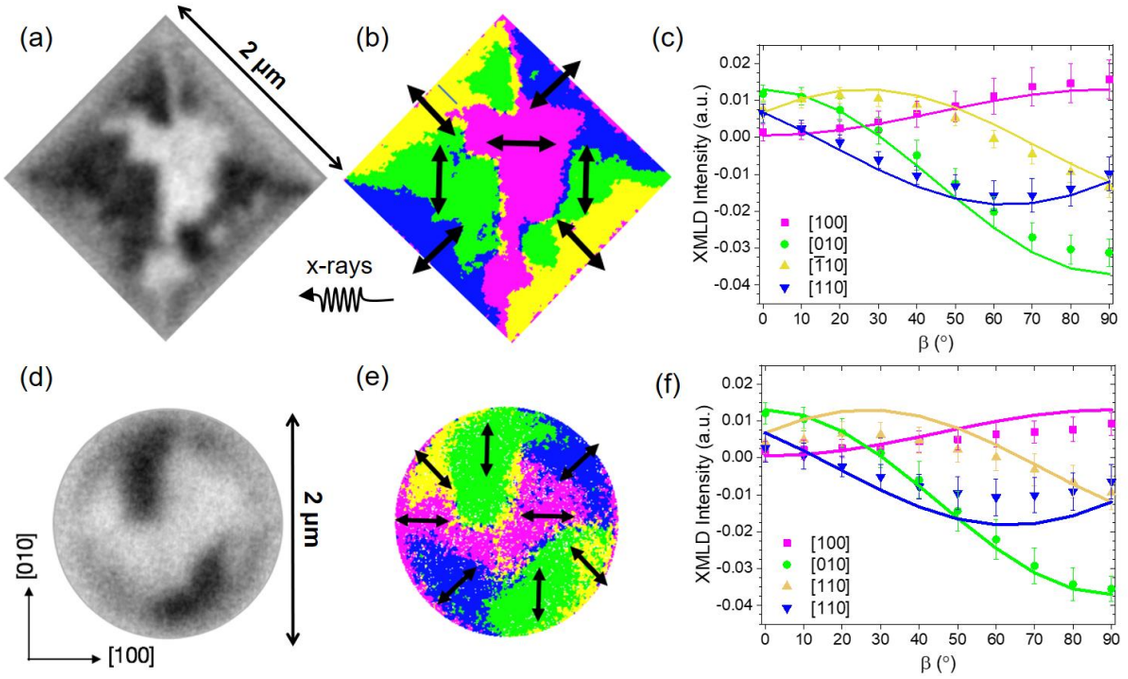


**Figure 4.** (a) and (d) Fe XMLD-PEEM images at 105 K for $\beta = 90°$ of LSMO/LSFO micromagnets with varying shapes, (b) and (e) AFM domain maps where the arrows denote the orientation of the AFM spin axis, and experimental (filled symbols) and calculated (open symbols) XMLD intensity vs. $\beta$ curves for (c) square micromagnets with edges along <110> substrate directions and (f) circle micromagnets.

Cooling the patterned LSMO/LSFO superlattice below the $T_C$ of the LSMO layers allows the impact of exchange interactions between AFM and FM layers to be investigated. Fig. 5 compares the Fe XMLD with $\beta = 90°$ and Mn XMCD images obtained simultaneous from the same micromagnets at 36 K. The location of a dominant dark AFM domain is outlined with white dashed lines in all images for comparison. Regardless of shape, each dark AFM domain (with [010] AFM spin axis orientation) corresponds to small FM domains with dark/bright contrast (with $[010]$ and $[0\bar{1}0]$ FM magnetization orientations), while each bright AFM domain (with $[0\bar{1}0]$ AFM spin axis orientation) corresponds to FM domains with grey contrast (with $[100]$ and $[\bar{1}00]$ FM magnetization orientations). These domain orientations are consistent with a perpendicular relationship of the AFM spin axis and FM magnetization expected for a spin-flop coupled system. The small FM domains (0.1-0.3 µm in size) are consistent with X-PEEM images from 6-10 u.c. thick LSMO layers in unpatterned LSMO/LSFO superlattices and

LSMO/$LaFeO_3$ bilayers.[16, 17] The small domain size and much weaker Mn XMCD intensity likely arise from the ultrathin thickness, and prevents them from displaying prominent shape anisotropy effects. In contrast, micromagnets patterned in a 20 or 90 u.c. LSMO/10 u.c. $LaFeO_3$ bilayers displayed FM Landau patterns and a direct correlation between the FM and AFM domains.[17, 30] In those cases, the thicker LSMO layer dominated the FM and AFM domain patterns at low temperatures through spin-flop coupling, such that a reorientation of the AFM domain structure occurred above and below $T_C$ of the FM layer. In the patterned LSMO/LSFO superlattice, the AFM domains do not show any major changes between 300 K and 36 K besides the finer, stochastic details of the domain wall positions in the interior of the micromagnets (see Fig. S9). The thickness of the perimeter domains which maintain a perpendicular alignment with the micromagnet edge remains constant at ~0.30 μm regardless of measurement temperature crystallographic orientation and aspect ratio (Fig. S9). It is postulated that this perimeter region may be influence by the lateral strain imposed from the non-magnetic ion implanted matrix. In patterned LSMO micromagnets, this lateral strain was found to influence the magnitude of the FM magnetocrystalline anisotropy constant of the micromagnet perimeter.[35] Finally, the XMLD intensity vs. $\beta$ curves show the same trends, suggesting that the LSFO layer dominates the formation of AFM and FM domains as the temperature is decreased below $T_C$ of the FM layer. It should be noted that the lateral straggle from the $Ar^+$ ion implantation process used for patterning in this work is predicted to only extend 0.03 μm away from the edge of the Cr hard mask, eliminating it as a dominant source for the observed edge effects.

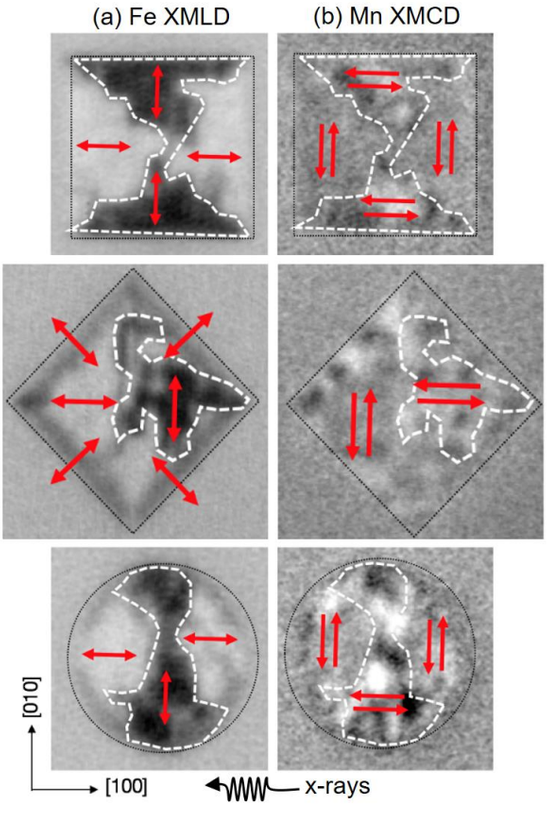


**Figure 5**: (a) Fe XMLD-PEEM with $\beta = 90$ ° and (b) Mn XMCD-PEEM images at 36 K from LSMO/LSFO micromagnets with varying shape showing the correlation between AFM and FM domains. Dashed lines denote the perimeter of AFM domains in the Fe-XMLD images and the corresponding area in the Mn-XMCD images. Arrows indicate the orientation of the magnetic spin axes of each domain.

## Conclusions

In summary, the effect of shape anisotropy on the AFM domain structure of micromagnets patterned into an LSFO thin film and LSMO/LSFO superlattice has been investigated using XMLD-PEEM microscopy. Only by capturing a series of images as a function of the polarization angle, $\beta$, ideally for two sample orientations, can the orientation of the AFM spin axis be fully determined. In LSFO thin films, four types of AFM domains exist with their spin axes canted out-of-plane by 35° +/- 5° with an in-plane projections along the <100> substrate directions. In micromagnets, magnetocrystalline anisotropy dominates for shapes with proportionally fewer edges aligned parallel to the easy axes while shape anisotropy gains importance when at least one extended edge of the micromagnet is aligned parallel to an AFM easy axis. In the limit of ultrathin LSFO layers in a LSMO/LSFO superlattice, the

AFM easy axis become the in-plane [100] and [010] substrate directions, and shape anisotropy effects dominate such that the orientation of pattern edges can be used to select specific AFM spin axes orientations parallel to any crystallographic direction. Therefore, due to this delicate balance between shape anisotropy, magnetocrystalline anisotropy, and exchange interactions, the AFM domain structure in LSFO micromagnets can be designed and manipulated for advanced AFM spintronic applications using parameters such as LSFO and LSMO layer thickness, micromagnet shape, and temperature.

**Supplementary Materials**

See supplementary materials for additional X-PEEM images from the LSFO thin films and LSMO/LSFO superlattices.

**Acknowledgements**

Funding for these experiments was obtained from the National Science Foundation (DMR 1411250 and 1745450). P.L. acknowledges the support of the John and Gina Wasson Honors Program at UC Davis. This research used resources of the Advanced Light Source, which is a Department of Energy (DOE) Office of Science User Facility under contract no. DE-AC02-05CH11231. A portion of this research was conducted at the Center for Nanophase Materials Sciences, which is a DOE Office of Science User Facility.

**Data Availability Statement**

The data that support the findings of this study are available from the corresponding author upon reasonable request.

References

1. Wadley, P., B. Howells, J. Železný, C. Andrews, V. Hills, R.P. Campion, V. Novák, K. Olejník, F. Maccherozzi, S.S. Dhesi, S.Y. Martin, T. Wagner, J. Wunderlich, F. Freimuth, Y. Mokrousov, J. Kuneš, J.S. Chauhan, M.J. Grzybowski, A.W. Rushforth, K.W. Edmonds, B.L. Gallagher and T. Jungwirth, *Electrical switching of an antiferromagnet.* Science, 2016. **351**(6273): p. 587.

2. Baltz, V., A. Manchon, M. Tsoi, T. Moriyama, T. Ono and Y. Tserkovnyak, *Antiferromagnetic spintronics.* Reviews of Modern Physics, 2018. **90**(1): p. 015005.

3. Jungwirth, T., X. Marti, P. Wadley and J. Wunderlich, *Antiferromagnetic spintronics.* Nature Nanotechnology, 2016. **11**(3): p. 231-241.

4. Marti, X., I. Fina and T. Jungwirth, *Prospect for Antiferromagnetic Spintronics.* IEEE Transactions on Magnetics, 2015. **51**: p. 2900104.

5. Jungfleisch, M.B., W. Zhang and A. Hoffmann, *Perspectives of antiferromagnetic spintronics.* Physics Letters A, 2018. **382**(13): p. 865-871.

6. Gomonay, O., V. Baltz, A. Brataas and Y. Tserkovnyak, *Antiferromagnetic spin textures and dynamics.* Nature Physics, 2018. **14**(3): p. 213-216.

7. Gomonay, O., T. Jungwirth and J. Sinova, *High Antiferromagnetic Domain Wall Velocity Induced by Neel Spin-Orbit Torques.* Physical Review Letters, 2016. **117**(1): p. 017202.

8. Shiino, T., S.-H. Oh, P.M. Haney, S.-W. Lee, G. Go, B.-G. Park and K.-J. Lee, *Antiferromagnetic Domain Wall Motion Driven by Spin-Orbit Torques.* Physical Review Letters, 2016. **117**(8): p. 087203.

9. Zubko, P., S. Gariglio, M. Gabay, P. Ghosez and J.-M. Triscone, *Interface Physics in Complex*

*Oxide Heterostructures.* Annu. Rev. Condens. Matter Phys., 2011. **2**: p. 141-165.

10. Takamura, Y., *Characterization of Antiferromagnetic/Ferromagnetic Perovskite Oxide Superlattices*, in *Nanostructured Materials for Magnetoelectronics*, B. Aktas and F. Mikailzade, Editors. 2013, Springer-Verlag: Berlin Heidelberg. p. 119-147.
11. Luning, J., F. Nolting, A.O. Scholl, H., J.W. Seo, J. Fompeyrine, J.-P. Locquet and J. Stohr, *Determination of the antiferromagnetic spin axis in epitaxial $LaFeO_3$ films by x-ray magnetic linear dichroism spectroscopy.* Phys. Rev. B, 2003. **67**: p. 214433.
12. Czekaj, S., F. Nolting, L.J. Heyderman, P.R. Willmott and G. van der Laan, *Sign dependence of the x-ray magnetic linear dichroism on the antiferromagnetic spin axis in $LaFeO_3$ thin films.* Phys. Rev. B, 2006. **73**: p. 020401(R).
13. Seo, J.W., E.E. Fullerton, F. Nolting, A. Scholl, J. Fompeyrine and J.-P. Locquet, *Antiferromagnetic $LaFeO_3$ thin films and their effect on exchange bias.* J. Phys.- Condens. Mat., 2008. **20**: p. 264014.
14. Koon, N.C., *Calculations of Exchange Bias in Thin Films with Ferromagnetic/Antiferromagnetic Interfaces.* Phys. Rev. Lett., 1997. **78**(25): p. 4865-4868.
15. Hinchey, L.L. and D.L. Mills, *Magnetic properties of ferromagnetic-antiferromagnetic superlattice structures with mixed-spin antiferromagnetic sheets.* Phys. Rev. B, 1986. **34**(3): p. 1689-1699.
16. Yang, F., N. Kemik, A. Scholl, A. Doran, A.T. Young, M.D. Biegalski, H.M. Christen and Y. Takamura, *Correlated domain structure in perovskite oxide superlattices exhibiting spin-flop coupling.* Physical Review B, 2011. **83**(1).
17. Bang, A.D., F.K. Olsen, S.D. Slöetjes, A. Scholl, S.T. Retterer, C.A.F. Vaz, T. Tybell, E.

Folven and J.K. Grepstad, *Magnetic domain formation in ultrathin complex oxide ferromagnetic/antiferromagnetic bilayers.* Applied Physics Letters, 2018. **113**(13): p. 132402.

18. Izumi, M., Y. Murakami, Y. Konishi, T. Manako, M. Kawasaki and Y. Tokura, *Structural characterization and magnetic properties of oxide superlattices $La_{0.6}Sr_{0.4}MnO_3/La_{0.6}Sr_{0.4}FeO_3$.* Phys. Rev. B, 1999. **60**: p. 1211-1215.

19. Arenholz, E., G. van der Laan, F. Yang, N. Kemik, M.D. Biegalski, H.M. Christen and Y. Takamura, *Magnetic Structure of $La_{0.7}Sr_{0.3}MnO_3$ / $La_{0.7}Sr_{0.3}FeO_3$ superlattices.* Appl. Phys. Lett., 2009. **94**: p. 072503.

20. Takamura, Y., F. Yang, N. Kemik, E. Arenholz, M.D. Biegalski and H.M. Christen, *Competing interactions in ferromagnetic/antiferromagnetic perovskite superlattices.* Physical Review B, 2009. **80**(18): p. 180417(R).

21. Folven, E., A. Scholl, A.T. Young, S. Retterer, J.E. Boschker, T. Tybell, Y. Takamura and J.K. Grepstad, *Effects of nanostructuring and substrate symmetry on antiferromagnetic domain structure in $LaFeO_3$ thin films.* Phys. Rev. B, 2011. **84**: p. 220410(R).

22. Bruno, F.Y., M.N. Grisolia, C. Visani, S. Valencia, M. Varela, R. Abrudan, J. Tornos, A. Rivera-Calzada, A.A. Ünal, S.J. Pennycook, Z. Sefrioui, C. Leon, J.E. Villegas, J. Santamaria, A. Barthélémy and M. Bibes, *Insight into spin transport in oxide heterostructures from interface-resolved magnetic mapping.* Nature Communications, 2015. **6**(1): p. 6306.

23. Li, Y.-Y., *Domain Walls in Antiferromagnets and the Weak Ferromagnetism of α-Fe2O3.* Physical Review, 1956. **101**(5): p. 1450-1454.

24. Czekaj, S., F. Nolting, L.J. Heyderman, K. Kunze and M. Kruger, *Antiferromagnetic domain configurations in patterned $LaFeO_3$ thin films.* J. Phys.- Condens. Mat., 2007. **19**: p. 386214.

25. Gomonay, H.V. and V.M. Loktev, *Shape-induced phenomena in finite-size antiferromagnets.* Physical Review B, 2007. **75**(17): p. 174439.

26. Gomonay, O., S. Kondovych and V. Loktev, *Shape-induced anisotropy in antiferromagnetic nanoparticles.* Journal of Magnetism and Magnetic Materials, 2014. **354**: p. 125-135.

27. Wu, J., D. Carlton, J.S. Park, Y. Meng, E. Arenholz, A. Doran, A.T. Young, A. Scholl, C. Hwang, H.W. Zhao, J. Bokor and Z.Q. Qiu, *Direct observation of imprinted antiferromagnetic vortex states in CoO/Fe/Ag(001) discs.* Nature Physics, 2013. **7**: p. 303-306.

28. Folven, E., Y. Takamura and J.K. Grepstad, *X-PEEM study of antiferromagnetic domain patterns in $LaFeO_3$ thin films and embedded nanostructures.* J. Electron Spectrosc. Relat. Phenom., 2012. **185**: p. 381-388.

29. Takamura, Y., R.V. Chopdekar, A. Scholl, A. Doran, J.A. Liddle, B. Harteneck and Y. Suzuki, *Tuning magnetic domain structure in nanoscale $La_{0.7}Sr_{0.3}MnO_3$ islands.* Nano Letters, 2006. **6**(6): p. 1287-1291.

30. Takamura, Y., E. Folven, J.B.R. Shu, K.R. Lukes, B.Z. Li, A. Scholl, A.T. Young, S.T. Retterer, T. Tybell and J.K. Grepstad, *Spin-Flop Coupling and Exchange Bias in Embedded Complex Oxide Micromagnets.* Physical Review Letters, 2013. **111**(10): p. 107201.

31. Folven, E., A. Scholl, A.T. Young, S.T. Retterer, J.E. Boschker, T. Tybell, Y. Takamura and J.K. Grepstad, *Crossover from Spin-Flop Coupling to Collinear Spin Alignment in Antiferromagnetic/Ferromagnetic Nanostructures.* Nano Letters, 2012. **12**: p. 2386-2390.

32. Folven, E., T. Tybell, A. Scholl, A. Young, S.T. Retterer, Y. Takamura and J.K. Grepstad, *Antiferromagnetic Domain Reconfiguration in Embedded $LaFeO_3$ Thin Film Nanostructures.*

Nano Letters, 2010. **10**(11): p. 4578-4583.

33. Bang, A.D., I. Hallsteinsen, R.V. Chopdekar, F.K. Olsen, S.D. Slöetjes, K. Kjærnes, E. Arenholz, E. Folven and J.K. Grepstad, *Shape-imposed anisotropy in antiferromagnetic complex oxide nanostructures.* Applied Physics Letters, 2019. **115**(11): p. 112403.

34. Bang, A.D., I. Hallsteinsen, F.K. Olsen, S.D. Slöetjes, S.T. Retterer, A. Scholl, E. Arenholz, E. Folven and J.K. Grepstad, *Néel vector reorientation in ferromagnetic/antiferromagnetic complex oxide nanostructures.* Applied Physics Letters, 2019. **114**(19): p. 192403.

35. Lee, M.S., T.A. Wynn, E. Folven, R.V. Chopdekar, A. Scholl, A.T. Young, S.T. Retterer, J.K. Grepstad and Y. Takamura, *Controlling spin textures in complex oxide microstructures* ACS Nano, 2016. **10**: p. 8545-8551.

36. Kumigashira, H., D. Kobayashi, R. Hashimoto, A. Chikamatsu, M. Oshima, N. Nakagawa, T. Ohnishi, M. Lippmaa, H. Wadati, A. Fujimori, K. Ono, M. Kawasaki and H. Koinuma, *Inherrent charge transfer layer formation at $La_{0.6}Sr_{0.4}FeO_3/La_{0.6}Sr_{0.4}MnO3$ heterointerfaces.* Appl. Phys. Lett., 2004. **84**: p. 5353-5355.

37. Doran, A., M. Church, T. Miller, G. Morrison, A.T. Young and A. Scholl, *Cryogenic PEEM at the Advanced Light Source.* Journal of Electron Spectroscopy and Related Phenomena, 2012. **185**: p. 340-346.

38. Lee, J.S., D.A. Arena, P. Yu, C.S. Nelson, R. Fan, C.J. Knane, S. Langridge, M.D. Rossel, R. Ramesh and C.-C. Kao, *Hidden Magnetic Configuration in Epitaxial $La_{1-x}Sr_xMnO_3$ Films.* Phys. Rev. Lett., 2010. **105**: p. 257204.

39. Scholl, A., J. Stohr, J. Luning, J.W. Seo, J. Fompeyrine, H. Siegwart, J.-P. Locquet, F. Nolting, S. Anders, E.E. Fullerton, M.R. Scheinfein and H.A. Padmore, *Observation of*

*antiferromagnetic domains in epitaxial thin films.* Science, 2000. **287**: p. 1014-1016.

Journal of Applied Physics





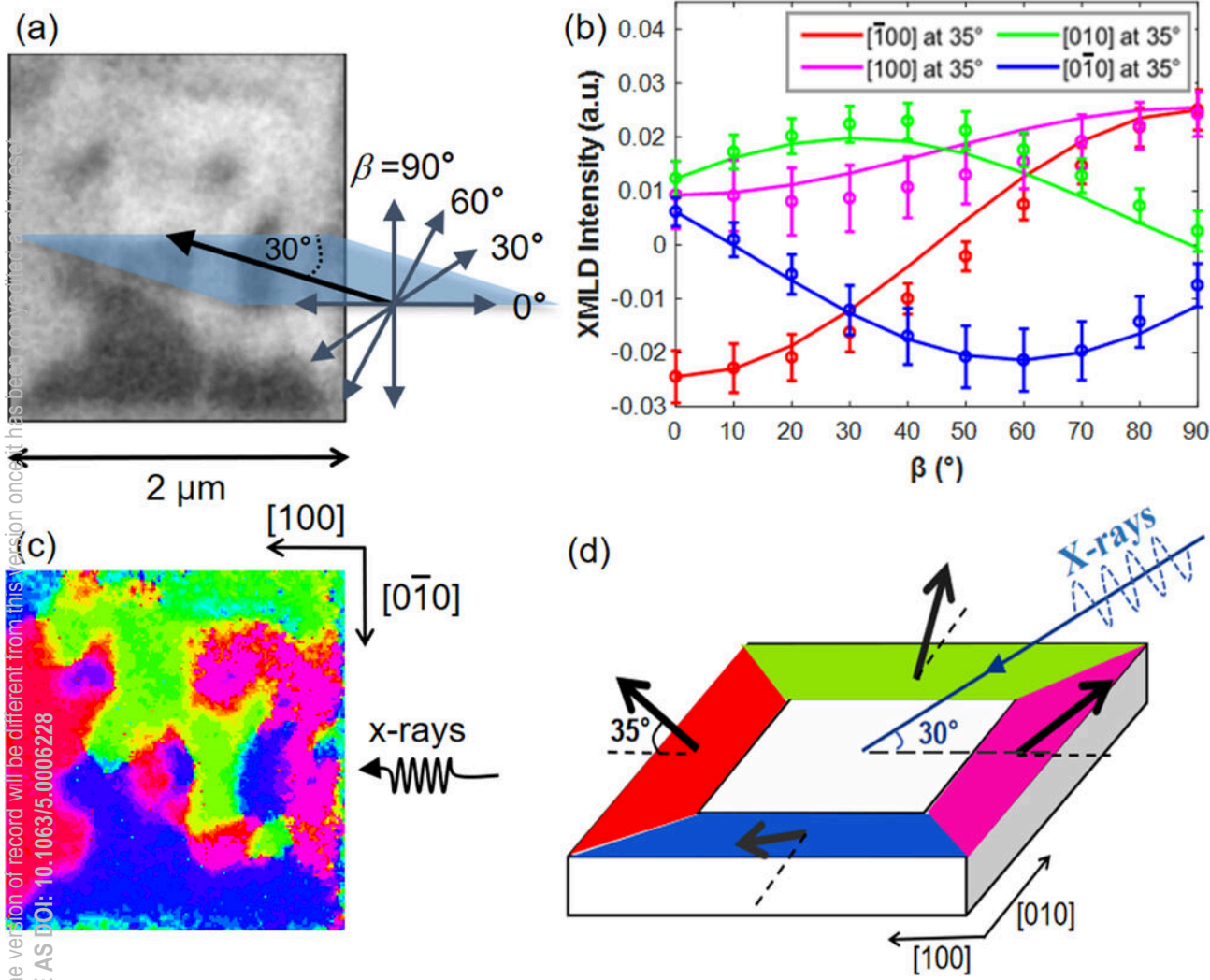

AIP Publishing

Journal of Applied Physics

ACCEPTED MANUSCRIPT



PLEASE CITE THIS ARTICLE AS DOI: 10.1063/5.0006228

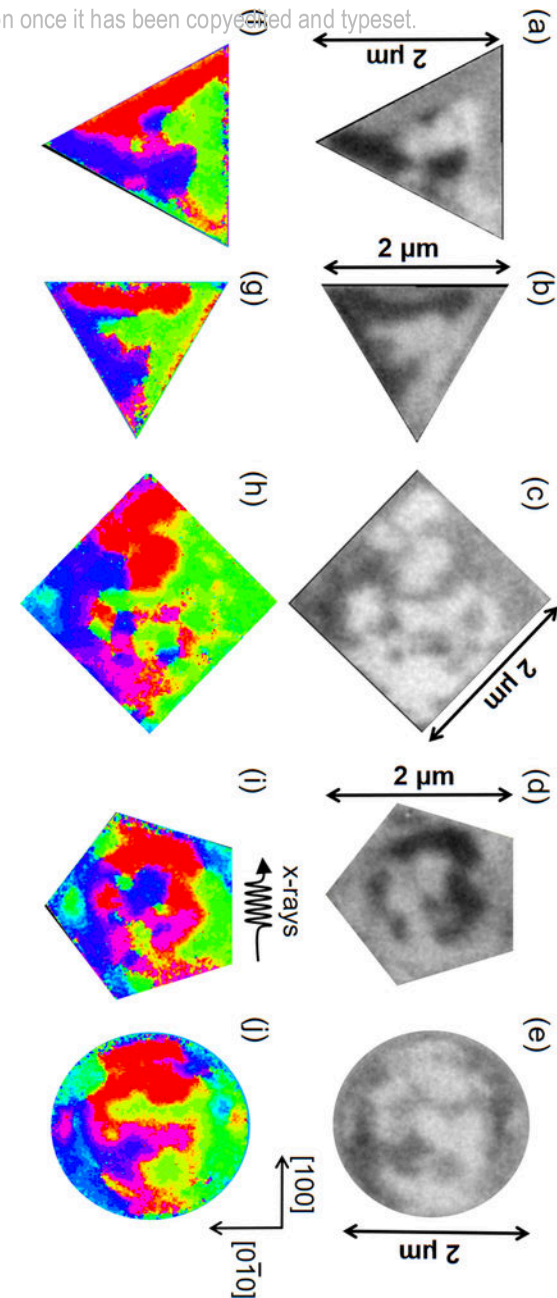

Journal of Applied Physics



PLEASE CITE THIS ARTICLE AS DOI: 10.1063/5.0006228

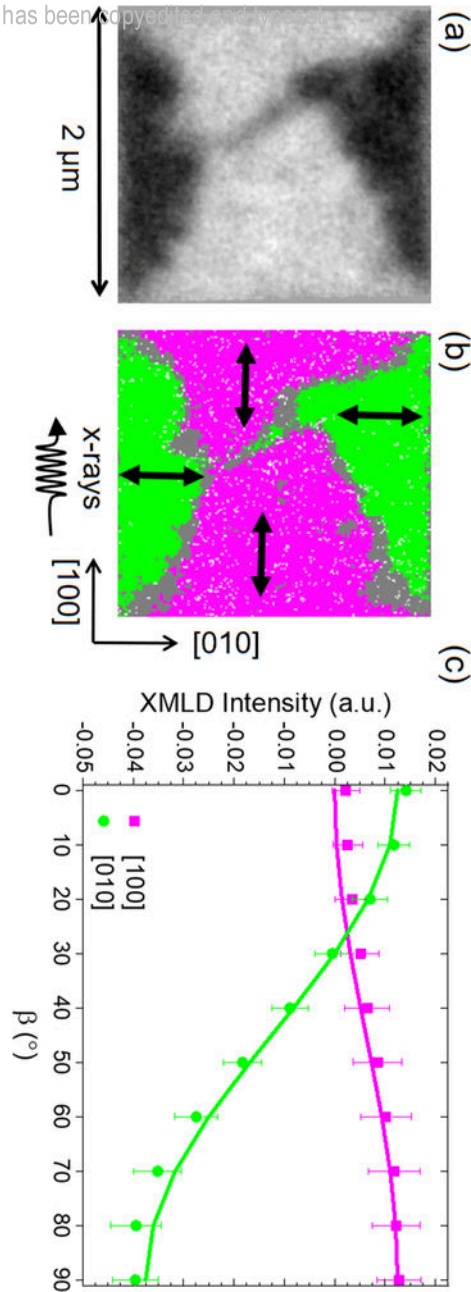

PLEASE CITE THIS ARTICLE AS DOI: 10.1063/5.0006228

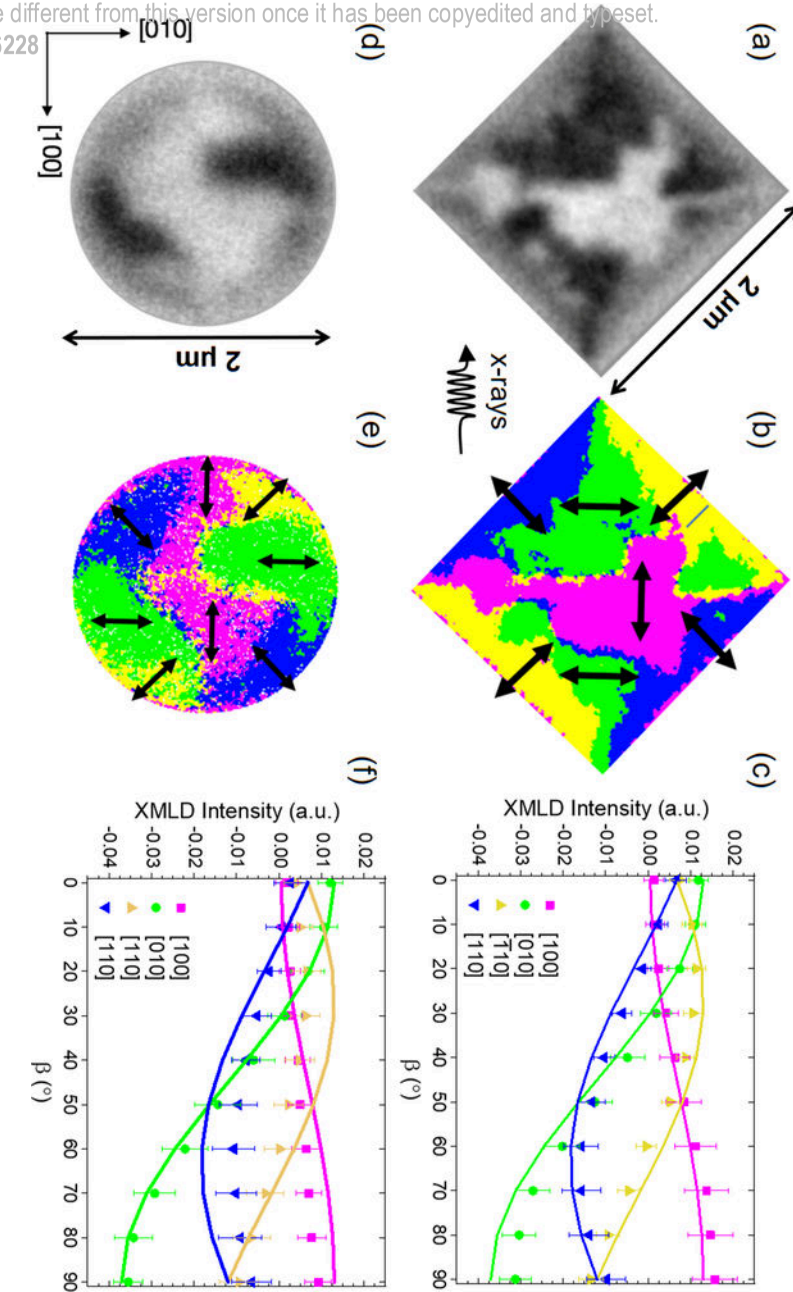

AIP Publishing

Journal of Applied Physics

ACCEPTED MANUSCRIPT



PLEASE CITE THIS ARTICLE AS DOI: 10.1063/5.0006228